THE ASTROPHYSICAL JOURNAL, 460:506–521, 1996 March 20

EVIDENCE FOR WIND ATTENUATION AND A MULTITEMPERATURE PLASMA IN THE COMBINED *EUVE* AND *ROSAT* OBSERVATIONS OF ϵ CANIS MAJORIS (B2 II)

D. H. COHEN,[1] R. G. COOPER,[1] J. J. MACFARLANE,[1,2] S. P. OWOCKI,[3]
J. P. CASSINELLI,[1] AND P. WANG[2]

Received 1995 August 10; accepted 1995 September 28

ABSTRACT

We use both *EUVE* and *ROSAT* data sets to test three general pictures—coronal, wind shock, and external—for the production of the observed high-energy emission from the B giant, ϵ CMa (B2 II). Because of the very low interstellar opacity along its line of sight, ϵ CMa is the only early-type star that has strong emission lines detected with the *EUVE* spectrometers. The line spectrum provides the first solid observational evidence that the emission is thermal. Theoretical EUV spectra based upon two-temperature model fits to the *ROSAT* data predict too much flux, especially in the iron line complex near 175 Å. We use progressively more complex models until we are able to achieve a fit to the combined data sets. We find that both a temperature distribution in the emitting plasma and some attenuation of the EUV and soft X-ray emission by the ionized stellar wind must be included in the models. The model fitting indicates that only 13% to 21% of the emission-line complex near 175 Å escapes the wind. This amount is consistent with the wind shock model, in which the emitting material is distributed throughout the stellar wind. It is much more absorption than is predicted by the external source model, where all of the emitting material is at radii beyond the cold stellar wind. And it is significantly less absorption than is expected in the coronal model, given what is known about the star's mass-loss rate. The derived temperature distribution and wind filling factor of hot gas are also qualitatively consistent with our numerical simulations of wind shocks. We conclude that although the observed flux from ϵ CMa in the interval 54 eV $< E <$ 100 eV is approximately the same as that above 100 eV, because of wind attenuation the total generated radiation in the EUV band between 54 eV and 100 eV is 5 times greater than that in the X-ray region.

Subject headings: radiation mechanisms: thermal — stars: early-type — stars: individual (ϵ Canis Majoris) — stars: mass loss — ultraviolet: stars — X-rays: stars

1. INTRODUCTION

With the launch of the *Einstein* X-ray telescope early-type stars were identified as a new class of soft X-ray emitters (Harnden et al. 1979; Seward et al. 1979). Subsequent studies have shown that the X-ray luminosities obey the law $L_X/L_{Bol} \approx 10^{-7}$ for essentially all O stars (Pallavicini et al. 1981; Long & White 1980; Chlebowski, Harnden, & Sciortino 1989) and for very early B stars (Grillo et al. 1992; Cassinelli et al. 1994). Stars later than about B2 have also been found to be X-ray emitters, but with a lower mean L_X/L_{Bol} and with a larger dispersion about the mean (Meurs et al. 1992; Cassinelli & Cohen 1994; Berghöfer & Schmitt 1994; Cohen et al. 1996). Despite the existence of a large observational database, no completely satisfactory model exists for the production of X-rays across all O and B spectral subtypes and luminosity classes, and the 10^{-7} law has not been explained.

Even before these detections, coronal X-ray emission was proposed to explain the superionization that is seen in the UV spectra of OB stars (Cassinelli & Olson 1979). A potential coronal heating mechanism for early-type stars was first proposed by Hearn (1972) and a hybrid coronal and wind model was discussed by Waldron (1984). Possible evidence for X-ray emission from magnetically confined regions in very young late B stars has recently been put forward (Schmitt et al. 1993). Transient X-ray activity of a possibly magnetic/coronal origin has been detected on the Be star λ Eri (Smith et al. 1993). However, no process known to operate in early-type stars has been shown to generate and sustain X-ray–emitting coronae. Furthermore, various studies have limited the extent, temperature, and the fractional contribution to the total X-ray output of purported coronal zones in O stars (Cassinelli, Olson, & Stalio 1978; Nordsieck, Cassinelli, & Anderson 1981; Cassinelli & Swank 1983; Baade & Lucy 1987; MacFarlane et al. 1993). It appears that some mechanism other than emission from a corona must account for a significant fraction of the X-ray luminosity in O stars.

Several wind shock models have been discussed over the years. Lucy & White (1980) and Lucy (1982) proposed empirical wind shock models to explain the observed X-rays in early-type stars. The periodic shock model of Lucy (1982) is motivated by the radiation force instability (or wind instability) mechanism which had earlier been suggested by Lucy & Solomon (1970). Lucy's model, though conceptually based on the instability mechanism, is an empirical one, with the only free parameter, v, being the velocity increment (in sound speed units) between sequential velocity peaks of the assumed multishock wind structure. Lucy argued that $v \approx 1$ but observations of several O stars showed that the value of v must be well above unity in order to match the observed X-ray flux (Lucy 1982; Cassinelli & Swank 1983). The physics of the radiation force instability mechanism was investigated in depth by Owocki &

[1] University of Wisconsin—Madison, Department of Astronomy, 475 North Charter Street, Madison, WI 53706; cohen@duff.astro.wisc.edu.
[2] University of Wisconsin—Madison, Fusion Technology Institute, 1500 Johnson Drive, Madison, WI 53706.
[3] Bartol Research Institute, University of Delaware, Newark, DE 19716.

Rybicki (1984) and by Owocki, Castor, & Rybicki (1988) who showed that radiation-driven winds are inherently unstable and that the instability leads to a chaotic wind structure with many shock zones distributed throughout the outer regions of the stellar wind. These authors made no predictions of X-ray emission, however, because their numerical simulations assume an isothermal flow. The energy balance in wind shocks was investigated by MacFarlane & Cassinelli (1989) who considered a driven wave shock propagating through the stellar wind. Although these authors used a complete energy equation which included expansion cooling, radiative cooling, and conduction, the dynamics of the wind instability mechanism were not included. Instead they imposed the shock jump conditions directly into their simulations by discontinuously changing the velocity profile of the stellar wind. Another wind shock mechanism was proposed by Mullan (1984) who postulated that in the reference frame of a rapidly rotating star density enhancements in the wind should lag behind the surface of the star and could interact with each other, possibly producing shocks, hot plasma, and associated X-ray emission. Numerical simulations show that such density contrasts can form above star spots and lead to wind shocks (Cranmer & Owocki 1995).

Recently the radiation force instability mechanism has been investigated with numerical simulations that do include the full energy equation (Cooper 1994; Feldmeier 1995). These simulations again reveal a highly structured and chaotic wind with many shocks distributed throughout the flow. There is typically a large distribution of shock strengths and hence plasma temperatures. As in the isothermal model of Owocki et al. (1988), a primary characteristic of these simulations is that most of the shocks are reverse shocks with fast moving rarefied material flowing into slower, denser shells. This leads to a morphology in which most of the wind material is cold and unshocked with the hot, shocked material representing only a small fraction of the available wind material. The general properties of these models agree reasonably well with the X-ray data from O stars (Cooper 1994). But B stars later than about B2 show more X-ray emission than the numerical simulations, and indeed than any wind shock model, can explain (Cooper 1994; Cassinelli et al. 1994). In spite of these difficulties, wind-shock models have emerged as the preferred mechanism of high-energy photon production in early-type stars due to the shortcomings of the coronal hypothesis, the firm physical foundation for the wind instability mechanism, and the mounting observational evidence for nonmonotonic velocity fields and clumpiness in hot star winds (see, e.g., Massa, Prinja, & Fullerton 1995, and references therein).

In all of the wind shock models the hot plasma is distributed throughout the wind and the emitted EUV and, to a lesser extent, X-ray radiation is subject to some degree of wind attenuation. The wind attenuation is much less severe for the wind shock models than for a base coronal model which has all of the hot plasma confined near the stellar surface. A third model, which makes predictions at the opposite extreme of wind attenuation, is the "terminal shock," or "external model," in which the outer regions of the wind are assumed to be completely hot. Although no specific heating mechanism has been proposed, this model is based on the expectation that in the relatively low density winds of B stars hot gas beyond a critical radius will never cool radiatively. This can lead to a cessation of the radiation driving of the wind as the gas in the wind becomes very highly ionized (Abbott & Friend 1989) and may produce a wind morphology in which a cool interior region is completely surrounded by an extended hot outer layer (Drew, Denby, & Hoare 1994; Porter & Drew 1995). In this picture the high-energy photons emitted from the terminal shock zone are subject to little or no wind attenuation. In summary, there are three general morphologies which can be distinguished by the degree of wind attenuation. We refer to these three distinct morphologies with the labels "coronal," "wind shock," and "external."

There is a large and growing database of high-energy observations of early-type stars. The data from the *Einstein* IPC and *ROSAT* PSPC are at energies above 100 eV, where much of the emission from hot ($T > 10^6$ K) plasma is radiated. However, the spectral resolution is rather low ($\lambda/\Delta\lambda \approx 1$ and 3 for *Einstein* and *ROSAT*, respectively). Therefore the spectral fitting models used for data analysis have been very basic. Usually the source is assumed to be characterized by just one temperature and no wind opacity is included in the fitted models. In these cases the source temperature, the emission measure and a column density of interstellar material are adjusted to achieve a fit. Occasionally a two-temperature source model is used. The study of the *ROSAT* observations of ζ Puppis (O4 f) by Hillier et al. (1993) is one of the few observational studies in which stellar wind attenuation using opacities appropriate for the wind conditions is considered in combination with a two-temperature emission model. Although these data have low spectral resolution, they have very high signal to noise, and better fits are achieved when the authors include wind attenuation in their models than when they do not. Recently, some moderate-resolution ($\lambda/\Delta\lambda \approx 10$) X-ray data from O stars have become available from BBXRT (Corcoran et al. 1993) and *ASCA* (Corcoran et al. 1995). These data show improved observational evidence for X-ray attenuation by the stellar wind. Although these analyses make use of realistic stellar wind opacities, the emission models have only two discrete source temperatures and do not account for the spatial distribution of the emitting plasma in the wind.

In contrast to the O stars, which have winds that are optically thick to X-rays out to tens or even hundreds of stellar radii, the winds of B stars are only marginally thick. We can therefore directly detect X-rays from most of the emitting volume in the winds of B stars. This observational advantage for B stars over O stars is welcome because the B star winds are less well understood than those of the O stars. Cassinelli et al. (1994) and Cohen et al. (1996) derived extremely large X-ray filling factors for near-main-sequence B (or B V) stars, and suggested either that some nonwind emission mechanism was operating, or that the theoretical mass-loss rates for B V stars have been underestimated. Observational determinations of mass-loss rates are much more uncertain for B stars than for O stars because B stars do not show UV resonance lines that are as strong as those in O stars, nor are the stars detected at radio wavelengths, with the exception of the hypergiant B stars such as P Cygni. The B giant star, ϵ CMa, which we discuss in this paper, is intermediate in mass-loss rate and wind density between the O stars and the B V stars.

The program star, ϵ CMa, is the only early-type star with strong short-wavelength emission lines detected by *EUVE*. Two *EUVE* observations are used in this study. The first has been reported by Cassinelli et al. (1995). To increase the

signal-to-noise ratio a second observation was made a year after the first. This second *EUVE* observation has not been reported upon previously. Data from both observations spanning the wavelength range 80 Å $< \lambda <$ 360 Å are used for the analysis described in this paper. The *ROSAT* data include observations taken both with and without the boron filter. Combining the *EUVE* and *ROSAT* data sets provides two clear advantages over the analysis of low-resolution X-ray data alone: due to the moderate resolution of *EUVE* ($\lambda/\Delta\lambda \approx 250$) we are able to measure the strengths of individual, unblended emission lines of ions ranging from Fe IX to Fe XVI, each of which is a diagnostic of plasmas at a different temperature. In addition, the observed emission lines are subject to significant wind attenuation because photoionization cross sections are larger in the EUV than in the X-ray. Although detectors on the two satellites are sensitive to different photon energy ranges ($h\nu < 175$ eV for *EUVE* and 100 eV $< h\nu <$ 2400 eV for *ROSAT*), for the most part they probe the same gas. Many of the ion species which exist at temperatures of between 0.5 and 5 million K have several emission lines in the *ROSAT* energy range and several in the *EUVE* energy range. Therefore the combination of these two data sets is a very powerful tool for determining the properties of the hot plasma on ϵ CMa.

We analyze the combined data sets with the following goals in mind: To constrain the temperature distribution of the X-ray–emitting plasma, to quantify the degree of wind attenuation of the EUV photons and X-rays, and to determine the total amount of hot plasma necessary to account for the observed flux. The physical properties which we derive for the hot plasma on ϵ CMa will be useful to those modeling the X-ray production in this star and, by extension, in all early-type stars.

In § 2 we summarize the properties of ϵ CMa. In § 3 we describe the data sets used in this analysis and derive emission-line fluxes. In § 4 we describe results from fitting the combined data sets with traditional spectral models and outline the need for a model with both a temperature-dependent emission measure distribution and wind attenuation. We then describe the empirical model that provides good fits to both data sets and derive the extent of the solution space for this model. In § 5 we discuss the implications for the various models of high-energy emission in early-type stars and describe an initial calculation of a dynamical wind shock model for ϵ CMa. Conclusions are summarized in § 6.

2. THE STAR, ϵ CANIS MAJORIS

The MK standard Adhara, or ϵ CMa (B2 II), has been observed in every wavelength band from the mid-IR to X-ray, and its angular diameter has been measured at optical wavelengths using the Narrabri intensity interferometer (Hanbury Brown, Davis, & Allen 1974). This makes ϵ CMa one of the most completely observed early-type stars in the sky. From the angular diameter measurement and the near-complete wavelength coverage, the effective temperature and radius have been determined empirically. Combined with a measurement of the surface gravity these data also provide an empirical determination of the star's mass. Thus, ϵ CMa is an ideal object to use as a standard star for studies of the wind and high-energy properties of B stars. See Table 1 for a list of the stellar parameters.

The optical reddening of ϵ CMa is completely negligible because of the exceptionally low column density toward this object. Welsh (1991) has shown that ϵ CMa lies in the low-density interstellar tunnel centered on β CMa. In fact, ϵ CMa has even lower H I and He I column densities than does β CMa (Cassinelli et al. 1995; Cassinelli et al. 1996). Part of the sight line toward the star passes through the hot, tenuous gas often referred to as the "local bubble," but the sight line extends into a region which may be an extension of the bubble or may be photoionized by the B stars ϵ CMa and β CMa (Gry, York, & Vidal-Madjar 1985; Gry et al. 1996). It is the very low interstellar column density which makes the high-ionization emission lines of ϵ CMa observable in the EUV.

TABLE 1

STELLAR PARAMETERS FOR ϵ CANIS MAJORIS

Parameter	Value
Spectral type[a]	B2 II
m_V[a]	1.50
l, b[a]	240°, −11°
Distance[b] (pc)	188
θ_d[c] (mas)	0.80 ± 0.05
N_H[d] (cm^{-2})	0.7 to 1.2×10^{18}
T_{eff}[e] (K)	20990 ± 750
L_{Bol}[e] (ergs s^{-1})	1.2×10^{38}
log g[f] (cm s^{-2})	3.2 ± 0.15
$V \sin i$[g] (km s^{-1})	35
$\dot{M}$[h] ($M_\odot$ yr^{-1})	5.7×10^{-8}
v_∞[h] (km s^{-1})	910

[a] Bright Star Catalog: Hoffleit & Jaschek 1982.
[b] Bohlin, Savage, & Drake 1978.
[c] Hanbury Brown et al. 1974.
[d] Cassinelli et al. 1995.
[e] Code et al. 1976.
[f] Drew, Denby, & Hoare 1994.
[g] Uesugi & Fukuda 1982.
[h] Theoretical calculations based on the line list of Abbott 1982 and the fitting formula of Kudritzki et al. 1989.

The low ISM attenuation also makes it possible to observe the photospheric continuum of ϵ CMa below the Lyman edge with the *EUVE* spetrometers. It is one of only two early-type stars with a Lyman continuum observable with *EUVE*. In fact, in the long-wavelength *EUVE* bandpass it is the brightest nonsolar system source of any kind in the sky. The flux level in the Lyman continuum is 30 times greater than that predicted by LTE atmosphere models and substantially more than 30 times greater than the predictions of non-LTE models (Cassinelli et al. 1995). An infrared excess with respect to atmosphere models is also observed. The EUV and IR excesses can be naturally explained if the temperature exceeds the predictions of model atmospheres in the extreme outer layers of the photosphere, above log $m \approx -2$ (Cassinelli et al. 1995). It is not clear if there is a causal relationship between the EUV/X-ray field and the photospheric temperature excess, but the unexpectedly high continuum level certainly affects the ionization balance in the stellar wind, which in turn affects the wind attenuation of the X-rays.

The X-ray properties are quite typical of a late O or an early B star (Drew et al. 1994). Drew et al. (1994) found that the spectrum has both a soft component with $T \approx 1$–2×10^6 K and a harder component with $T \approx 5$–8×10^6 K. The X-ray luminosity is 10^{-7}, in agreement with the law for O stars. The X-ray flux and hardness ratios were found to vary no more than 20% on timescales of 20 minutes to 20

days. Although the authors interpreted the data within the context of the external model, we find that none of the three emission models can be positively ruled out by the *ROSAT* data alone.

The meaurement of the low-ionization emission lines which are seen in the *EUVE* spectrum of ϵ CMa also has relevance for our analysis. Cassinelli et al. (1995) detected strong emission in the He II Lyman α line at 304 Å and in the O III line at 374 Å. The latter line corresponds to the final line transition of the Bowen fluorescence mechanism. They showed that these lines cannot arise in either the photosphere or the million degree plasma which produces the X-rays, but must instead be formed in the cool, photoionized component of the stellar wind. Furthermore, the photoionization of He II by the EUV and X-ray field plays a crucial role in populating the upper levels of these transitions. In effect, almost all of the wind-absorbed EUV/X-ray photons ($h\nu > 54$ eV) get reprocessed into 304 Å and 374 Å line emission (MacFarlane, Cohen, & Cassinelli 1996). The analysis carried out by these authors confirms that the mass-loss rate is slightly more than $10^{-8}\ M_{\odot}\ \mathrm{yr}^{-1}$ and that the helium line is produced in regions extending to velocities of at least several hundred km s^{-1}.

3. THE DATA

We made use of two archival *ROSAT* PSPC observations and two *EUVE* observations of ϵ CMa, spanning 2 yr. We show a summary of the observations in Table 2. The *EUVE* observations were obtained as part of NASA's guest observer program, cycles 1 and 2.

The *ROSAT* data include both a boron-filtered spectrum and an unfiltered spectrum. The boron filter provides opacity above 188 eV and thus divides the lowest energy band in half and effectively increases the soft X-ray spectral resolution. The PSPC is a proportional counter and has a resolution that increases as $E^{1/2}$ with $E/\Delta E = 2.4$ at 930 eV (Truemper 1983; Pfeffermann et al. 1987). We extracted and reduced both *ROSAT* data sets using the MIDAS/EXSAS software. We used a circle of radius $\sim 6'$ to extract the source photons. Such a large area was necessary in order to encompass all of the "electronic ghost images" due to the very soft X-ray photons from the source. The electronic ghost image phenomenon occurs when the current induced by a low-energy photon on the cathode wires in the proportional counter is too weak to localize the photon's position within the two-dimensional detector and the position is interpreted as lying directly above one of the wires. Because the spacecraft wobble causes the mapping of detector and sky coordinates to change with time, the misinterpretation of soft photon positions within the detector can lead to a spurious spatial extension of the soft X-ray image along one axis in the plane of the sky (Nousek & Lesser 1993). The background was sampled from a nearby area on the detector which was devoid of other point sources. The background was then subtracted and the resulting data were divided into 10 energy bins such that each bin has roughly the same number of counts.

TABLE 2

OBSERVATIONS

Instrument	Observation Dates	Exposure Time (s)
ROSAT (unfiltered).....	1992 Mar 23–Apr 15	2290
ROSAT (boron).....	1992 Mar 17–Apr 15	9213
EUVE year 1	1993 Jan 17–19	62323[a]
EUVE year 2	1994 Mar 8–12	142227[a]

[a] The effective exposure time for the MW spectrometer.

The *EUVE* instrument has a grazing incidence mirror with a grating incorporated into a slitless spectrograph design. The photons are registered in one of three spectrometers by stacked microchannel plates (Bowyer & Malina 1991). The *EUVE* telescope therefore has characteristics of both X-ray and UV instruments. For this paper we make use of the short- and medium-wavelength spectrometer data, which effectively cover the wavelength ranges 70–180 Å and 170–365 Å. The FWHM spectral resolutions are approximately 0.5 and 1.0 Å in the two spectrometers. We used the CEA software for *EUVE* data analysis (version 1.4), which runs inside IRAF. We sampled the background spectrum in strips above and below the source spectrum on the detectors, and then subtracted it from the source. Deadtime and telemetry saturation ("primbsching") corrections were made in order to calculate an effective exposure time for each spectrometer. The analysis of the extracted *EUVE* and *ROSAT* spectra takes place outside of IRAF, as we describe in the next section.

In order to compare the data with models we extracted the line stengths and the upper limits of the nondetected lines in the *EUVE* data. The photospheric continuum emission, which extends down to the He II edge at 228 Å, was fitted in the vicinity of each line with a second-order polynomial and subtracted from the data. We then measured the line strengths by summing the counts across the observed lines (typically over a region with a breadth of twice the FWHM resolution). The statistical errors (including those due to the continuum fit and subtraction) were propagated. The fluxes were determined by dividing the data by the tabulated effective areas. We used these procedures to extract line fluxes for the two individual *EUVE* observations as well as for the sum of the two. See Table 3 for the line fluxes. The medium wavelength spectrometer data are shown in Figure 1. All five of the emission lines are seen in this detector and the effective area is quite constant, so the count rates reflect the relative flux levels. None of the five lines has energies above 100 eV (124 Å), and therefore they do not contribute to the *ROSAT* flux.

We consider for our analysis only lines which are detected at least at the 4 σ level. There are several features which are marginally detected ($\approx 3\ \sigma$ significance). The strongest case is a broad line blend near 185 Å which, taken as a whole, is detected at the 4 σ level. Unfortunately, this broad feature has contributions from several ion stages of iron which are formed over a wide range of temperatures, and the individual lines fluxes cannot be measured.

The Fe XII lines near 193 Å and 195 Å are the undetected lines that one would have expected to be the strongest. These Fe XII lines are among the strongest iron lines in the Solar EUV Rocket Telescope and Spectrograph (SERTS) solar EUV (170–450 Å) spectrum (Thomas & Neupert 1994). Although the intensity of these lines is on par with that of the Fe IX 171 Å line in the SERTS spectrum, it is not so surprising that the Fe XII lines are not seen in the ϵ CMa spectrum. There are three reasons for this: The lines have emissivities a little less than that of the 171 Å line (Raymond & Smith 1977; Mewe, Gronenschild, & van den Oord 1985; Landini & Monsignori-Fossi 1990), they are formed at

TABLE 3

EUVE HIGH ION EMISSION LINES

Ion	λ (Å)	log $T(\epsilon_{max})$[a]	Detector	Counts yr 1 + 2	Flux[b] (10^{-13} ergs s^{-1} cm^{-2}) yr 1	yr 2	1 + 2	F_2/F_1[c]	Luminosity[d] (10^{29} ergs s^{-1})
Fe IX	171.1	5.90	SW	74 ± 15	1.7	1.1	1.3	0.7	6.9
			MW	115 ± 18	1.1[e]	1.4	1.3	1.3	6.9
Fe X.....	174.5	6.01	SW	46 ± 14	0.8[e]	1.2	0.8	1.5	4.3
			MW	76 ± 16	0.8[e]	0.8	0.8	1.0	4.3
Fe XI	180.6	6.09	MW	77 ± 17	1.0	0.6	0.8	0.6	4.4
Fe XV	284.2	6.32	MW	137 ± 18	1.0	1.5	1.3	1.5	10.3
Fe XVI.....	335.4	6.45	MW	102 ± 20	0.6	0.8	0.7	1.3	7.4

[a] Temperature of maximum emissivity in the Raymond & Smith 1977 equilibrium model.
[b] At the top of the Earth's atmosphere.
[c] Ratio of the flux detected in the second year's observation to that detected in the first year.
[d] Corrected for ISM absorption with $N_{H\,I} = 1 \times 10^{18}$, $N_{He\,I} = 1.5 \times 10^{17}$, and $N_{He\,II} = 0.5 \times 10^{17}$.
[e] Detections only at the 2 σ level.

slightly higher temperatures where there is less plasma (see § 4.4), and they are closer to the He II edge and are therefore subject to more attenuation.

The absolute calibration of the *EUVE* spectrometers is reported to be good to about 25%, although the relative calibration between different pixels in one spectrometer is considerably better (Boyd et al. 1994; Vallerga et al. 1994). As can be seen in Table 3, there are two lines measured in both the short- and medium-wavelength spectrometers. The fluxes agree only to about 25%, even after accounting for statistical uncertainties.

Table 3 also shows that the fluxes in each line remain constant between the first and second years of observations. The observed degree of variation in each EUV line from the first observation to the second is, in most cases, consistent with the quoted statistical uncertainties. None of the five lines varied by more than 50% between the two observations. This remarkable degree of constancy in line luminosity for lines created over a range of temperatures implies that the properties of the hot plasma are quite constant over time and is, in fact, what justifies simultaneously fitting all of the data sets.

4. DATA ANALYSIS

In analyzing broadband X-ray data, compromises must be made between increasing the accuracy of spectral models

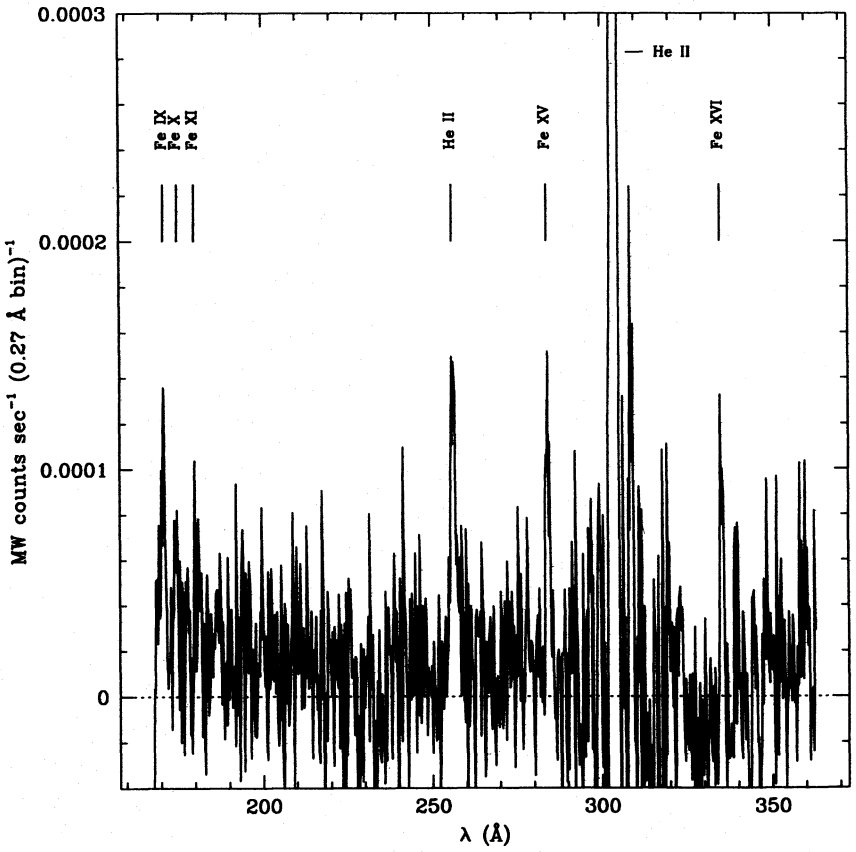

FIG. 1.—Combined yr 1 and yr 2 *EUVE* medium-wavelength spectrometer data. The effective exposure time is 204,550 s. The five iron emission lines are identified, along with the two He II emission lines. The displayed data are continuum subtracted for $\lambda > 228$ Å.

on the one hand, and keeping the numbe of free parameters to a reasonable minimum on the other. Crude, unrealistic models often provide adequate fits to low-resolution X-ray data. When better quality data are introduced, the crude models tend to fail and more realistic models must be constructed to fit the data. Until now, this process has progressed further for late-type stars than for early-type stars. As outlined in the Introduction, even the highest signal-to-noise, highest resolution data previously available for early-type stars can be fitted with simple two-temperature equilibrium models with local absorption included but radiation transfer effects neglected. In reality the high-energy emission from any class of stars probably has spatial, temporal, and spectral structure that is quite complicated. This is seen to be the case in the one star which can be spatially resolved with very high signal-to-noise—the Sun. Since stars cannot be spatially resolved at high energies, spatial information must be deduced from the spectral and temporal characteristics of the data.

To prevent overinterpretation of limited data sets, we believe in using a conservative method of model fitting, in which the complexity of the model is gradually increased until an adequate fit between model and data is achieved. We therefore first consider the *ROSAT* and *EUVE* data separately using relatively basic, traditional model-fitting techniques for X-ray and UV data. Next we test whether these simple models can *simultaneously* fit the combined data sets, and if not, we consider more realistic models.

4.1. *One- and Two-Temperature Fits to the ROSAT Data*

As we describe in the Introduction, X-ray data have historically been fitted with one- and two-temperature optically thin equilibrium models. No reasonable physical models predict the presence of one or two totally isothermal plasmas, but the assumption is that the derived temperatures reveal something about the dominant temperatures of the various regions of hot plasma or about the plasma temperature distribution in the largest physical structures. Simple models are necessary because X-ray spectral data typically contain fewer than 10 independent resolution elements. In fact, there are no X-ray observations of B stars for which even the hypothesis of thermal line emission can be unambiguously confirmed. The *ROSAT* observations of ϵ CMa shown in Figure 2 are no exception. These data are, however, high signal-to-noise, and the presence of both boron-filtered and unfiltered spectra provides more independent information than either one alone can.

Because the *ROSAT* PSPC is a low-resolution instrument, the predicted fluxes must be convolved with the spectral response matrix of the detector and then compared to the observations. The fluxes are predicted from models of the plasma emissivity as follows:

$$f_\lambda = e^{-\tau_\lambda(\mathrm{ISM})} \frac{L_\lambda}{4\pi D^2}, \tag{1}$$

$$L_\lambda = \int n_e n_\mathrm{H} \Lambda(T, \lambda) dV, \tag{2}$$

where the emissivity, Λ (ergs cm^3 s^{-1}), describes the spectral energy distribution per unit emission measure as a function of temperature in, e.g., the Raymond and Smith (1977) plasma code, n (cm^{-3}) is the particle density in the emitting plasma, D is the distance, and τ_λ(ISM) is the interstellar optical depth. In general, there is a distribution of temperatures within the emitting plasma so that effectively the emission measure, EM $= \int n_e n_\mathrm{H}\, dV$ is a function of temperature. A weighting function, $Q(T)$, which is the differential emission measure, and can be thought of as the temperature distribution of the emitting plasma, is defined by

$$Q(T)dT = n_e n_\mathrm{H} dV = d\mathrm{EM}, \tag{3}$$

so that

$$L_\lambda = \int Q(T)\Lambda(T, \lambda) dT. \tag{4}$$

Note that this integral is over the temperature distribution in the plasma, not the photon energy. The factor $Q(T)$ is normalized so that an integral over temperature gives the total emission measure.

We start by fitting the combined filtered and unfiltered *ROSAT* data sets with a one-temperature model, $Q(T) = \mathrm{EM}_1\, \delta(T - T_1)$, having two free parameters, the temperature, T_1, and the emission measure, EM_1. We know the interstellar column densities relatively well, and in any case they have a quite negligible effect in the *ROSAT* bandpass. The interstellar optical depth therefore is not a free parameter in our X-ray models. We find that one-temperature models are incapable of explaining the *ROSAT* data, in agreement with the finding of Drew et al. (1994).

We also consider two-temperature models, $Q(T) = \mathrm{EM}_1\, \delta(T - T_1) + EM_2\, \delta(T - T_2)$, having four free parameters. These models do provide adequate fits to the *ROSAT*

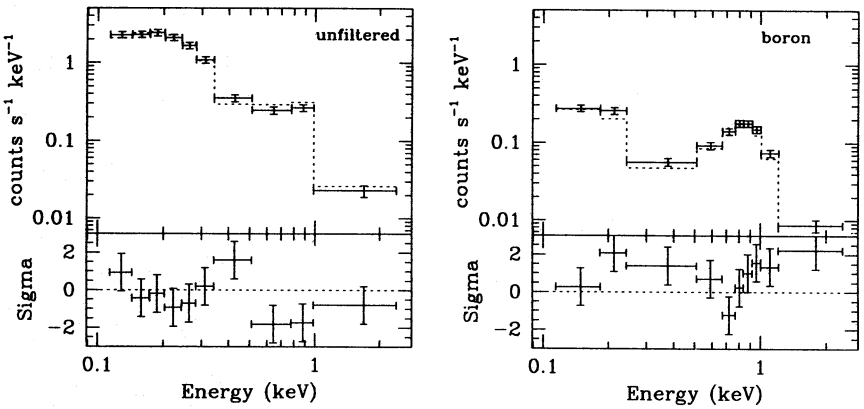

FIG. 2.—The left panel is the unfiltered *ROSAT* spectrum and the right panel is the spectrum taken with the boron filter. The ordinate represents the approximate central energies of each of the *ROSAT* bins. Note the small statistical uncertainty. The best-fit model (see § 5) is also shown (*dotted line*).

data. Like Drew et al. (1994), we find the solution space is centered near $T_1 = 1.5 \times 10^6$ K and $T_2 = 6 \times 10^6$ K, with similar emission measures for the two components.

4.2. *Analysis of EUV Line Spectrum*

Using this two-temperature *ROSAT* solution we predict fluxes for the five measured EUV lines. These predicted line fluxes, especially in the iron complex near 175 Å, are significantly larger than the observed fluxes (and larger than the upper limits for lines near 185 Å, 193 Å, 204 Å, and 211 Å as well). This is the first indication that simultaneous fitting of the *ROSAT* and *EUVE* data will require more detailed models.

Because of its significantly higher spectral resolution, *EUVE* data can be analyzed much like UV emission-line data of cool stars. In this method the strengths of individual lines are determined and upper limits for the emission measure as a function of temperature are calculated from the temperature-dependent ionization fractions, level populations, and transition probabilities (see, e.g., Brown et al. 1984). We chose this method as a first, semiquantitative attempt to understand the temperature distribution in the hot plasma. We used the Raymond & Smith code to predict the emissivity as a function of temperature for each of the five lines. The upper limits are given by

$$\mathrm{EM}(T) \lesssim \frac{L_{\mathrm{line}}}{\Lambda_{\mathrm{line}}} . \qquad (5)$$

These are upper limits because the emission measure at each temperature is calculated assuming an isothermal plasma at that temperature, while in reality there is a distribution of temperatures.

Plasma over a range of temperatures contributes to a given emission line. And because that range, or characteristic width, for a given line tends to be proportional to T the shape of the envelope of the EM(T) curves differs from $Q(T)$ by a factor of T^{-1}, $Q(T) \propto [\mathrm{EM}(T)/T]$. There is some confusion on this point in the literature and the term "differential emission measure" is sometimes taken to mean $(d\mathrm{EM})/d \log T$, which resembles the EM(T) curves (shown in Fig. 3) due to the extra factor of $1/T$ (see, e.g., Schmitt et al. 1990; but also Hartmann, Dupree, & Raymond 1982; Pan & Jordan 1995). Readers should be especially careful when comparing quoted slopes of power-law differential emission measure distributions.

The upper limits for EM(T) we calculate according to equation (5) and using the derived line luminosities from Table 3 are shown in Figure 3. The observed luminosities we use are corrected for interstellar absorption only. From this figure it appears that there is gas over a range of temperatures, and that more of it is hot ($T \lesssim 3 \times 10^6$ K) than warm ($T \lesssim 1 \times 10^6$ K). This interpretation assumes that any corrections for wind attenuation are negligible (but see § 4.4).

4.3. *Multitemperature Emission Fits to the Combined ROSAT and EUVE Data*

Although Figure 3 is suggestive, in order to quantitatively fit both the *ROSAT* and *EUVE* data we must calculate various models and compare them directly to both data sets. We use a goodness-of-fit indicator to define a solution space for the parameters of a given model. We start by calculating a grid of two-temperature models, the simplest model that fits the *ROSAT* data, and search the four-dimensional parameter space for the global best fit to the combined data. We then increase the complexity of the models until we are able to find a model which has intersecting solution spaces for the *ROSAT* and *EUVE* data. Once an acceptable type of model is identified our goal is to constrain the parameters of this model. This solution space—and the exclusion of large portions of parameter space—can tell us about the validity of the three general pictures of high-energy emission (coronal, wind shock, external). We then use the derived range of the model parameters to constrain the *physical* properties of the preferred picture of high-energy emission (such as the shock filling factor or, as in cool stars, the coronal loop covering factor).

Like the two-temperature models we use to fit the *ROSAT* data, the models we fit to the combined data sets are constructed from the Raymond & Smith (1977, 1993) plasma emission code assuming a density of $n_e = 10^{10}$ cm^{-3} (but see § 4.4). The interstellar opacity is calculated using the cross section tabulation of Morrison & McCammon

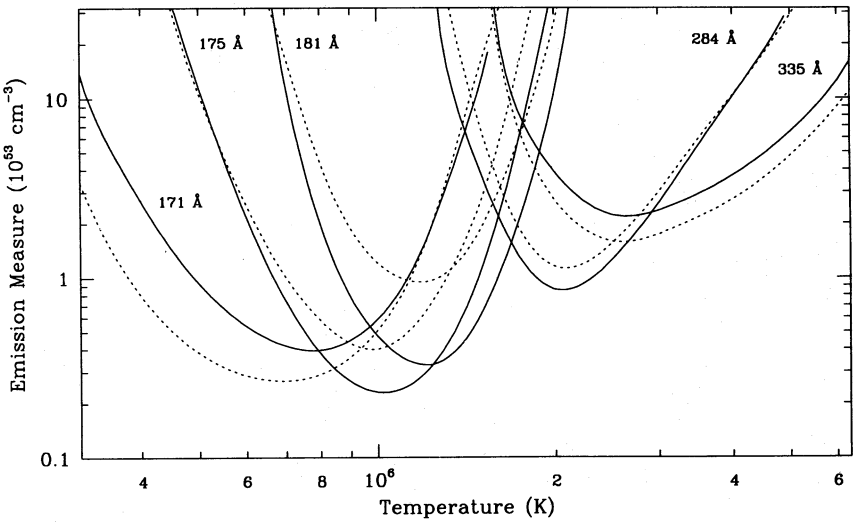

FIG. 3.—The lower extent of the solid curves represent the upper limit to the emission measure according to the Raymond & Smith (1977) code. The dotted lines are calculated using the Brickhouse, Raymond, & Smith (1995) revisions to the iron line emissivities.

(1983) plus a contribution from singly ionized helium (cross section from Rumph, Bowyer, & Vennes 1994). The neutral hydrogen column density along the sight line toward ϵ CMa is well constrained to 1×10^{18} cm^{-2} (Cassinelli et al. 1995), but the ionization state of the gas is not known. It is known that in general in the local interstellar medium hydrogen is partially ionized, as is helium (Vennes et al. 1994). We therefore assume that metals contribute to the opacity based on cosmic abundances, as defined by Morrison & McCammon (1983), and a *total* hydrogen column density of 2×10^{18} cm^{-2} (so that half of the hydrogen is assumed to be neutral and half is ionized). The interstellar helium ionization is somewhat uncertain and so we therefore consider two cases: (1) $N_{\rm He\ I} = 0.8 \times 10^{17}$ and $N_{\rm He\ II} = 1.2 \times 10^{7}$, and (2) $N_{\rm He\ I} = 1.5 \times 10^{17}$ and $N_{\rm He\ II} = 0.5 \times 10^{17}$. All of the models are compared to the data twice, once with each of these interstellar opacity models.

We use the Raymond & Smith plasma code because of its spectral coverage and because of its traditional use for fitting hot star X-ray data. Uncertainties in the plasma code must be taken into account when fitting the data. There are several other plasma emission codes available and we can get an idea of the uncertainty in the Raymond & Smith code by comparing different codes. In Figure 3 we show the upper limits we derive using the recent recalculation of the plasma emissivity for iron by Brickhouse, Raymond, & Smith (1995) in addition to those we derive from the Raymond & Smith (1977) tabulation. The Mewe et al. (1985) and Landini & Monsignori-Fossi (1990) codes show similar discrepancies for these five lines. There is better agreement among the different codes for the integrated fluxes in the relatively broad *ROSAT* energy bins than there is for individual EUV emission lines.

When fitting the *EUVE* data we require that the emission-line fluxes be reproduced to within a factor of 2 and that none of the upper limits is violated at the 4 σ level. These error tolerances account for the uncertainties associated with the plasma code as well as measurement uncertainties. If these criteria are met for all lines for a given set of model parameters, then we consider these parameters to constitute a solution for the *EUVE* data. For the *ROSAT* data we consider only photon-counting statistics in assigning formal uncertainties. The *ROSAT* goodness-of-fit indicator is the χ^2 statistic, which for an acceptable fit should not greatly exceed the number of degrees of freedom. Once the best-fit set of parameters for a given model is determined, the subset of parameter space which can be said with a specified probability to contain the "true" solution is found by applying the $\Delta\chi^2$ criterion for joint probability distributions (Lampton, Bowyer, & Margon 1976). It should be noted that while the goodness of fit for the *ROSAT* data is a matter of degree, the *EUVE* fitting criterion is binary—either a model is a good fit or it is not. We also stress that while the EUV radiation and X-ray radiation are separated in wavelength by a factor of a few to a factor of more than 10, they arise in the *same* plasma. In other words, an isothermal plasma emits photons over a wide range of energies.

We begin by recalculating two-temperature models with no wind attenuation, this time fitting the models to both the *ROSAT* and *EUVE* data sets. As we suspect from the *EUVE* model prediction of the best-fit *ROSAT* two-temperature model, we cannot achieve a fit to the combined data sets using this model. In fact, no *EUVE* solution exists at all for the parameters available in the two-temperature model.

Because Figure 3 suggests the presence of a range of temperatures in the emitting plasma, we next consider a model with a continuous differential emission measure. An arbitrary continuous differential emission measure would have too many free parameters to be a useful model, so we first use a power-law differential emission measure, $Q(T) \propto T^{\alpha}$ on a temperature interval $T = [T_{\rm min}:T_{\rm max}]$. This model has four free parameters—the slope, the two-temperature limits, and the total emission measure—which is no more than the cruder two-temperature model. Power-law differential emission measures are often fitted to X-ray observations of late-type stars, so it seems appropriate to try them to fit observations of early-type stars. The predicted luminosity in the power-law model is given by

$$L_{\lambda} = {\rm EM}_X K \int_{T_{\rm min}}^{T_{\rm max}} T^{\alpha} \Lambda(T, \lambda) dT \,, \qquad (6)$$

where the normalization constant, $K = (\alpha + 1)(T_{\rm max}^{\alpha+1} - T_{\rm min}^{\alpha+1})^{-1}$, and ${\rm EM}_X$ is the total emission measure of the EUV/X-ray–emitting gas.

The power-law emission model is also not able to provide a fit to the *EUVE* data. In order to test a more general continuous differential emission measure we next calculate four-temperature emission models, having eight free parameters. These models are meant to approximate an arbitrary differential emission measure, but to keep the number of free parameters to a minimum. Even the four-temperature model does not fit the *EUVE* data. As we find for the case of the two-temperature and the power-law models, the set of parameters which provide a good fit to the *ROSAT* data predict line fluxes in the iron complex near 175 Å which are several times larger than those observed. Furthermore, four-temperature models which correctly predict the fluxes for the five observed *EUVE* lines predict fluxes in lines with

TABLE 4

RESULTS OF FITS WITH DIFFERENT MODELS

Model Type	Free Parameters	*ROSAT* Fit (Best χ^2)	*EUVE* Fit	Combined Fit (Best *ROSAT* χ^2 in *EUVE* solution space)
1-Temperature	2	133	No	...
2-Temperature	4	22	No	...
Power-law	4	24	No	...
4-Temperature	8	16	No	...
1-Temperature + wind attenuation	3	133	No	...
2-Temperature + wind attenuation	5	22	Yes	41
Power-law + wind attenuation	5	21	Yes	25

180 Å $< \lambda <$ 228 Å which are too high. In Table 4 we list the different types of models we fit to the data and show the results for the *ROSAT* data, the *EUVE* data, and the combined data.

4.4. *Absorption plus Emission Models of the Combined Data*

It is clear that something in addition to the differential emission measure must be included in the models if we are to achieve an acceptable fit to all of the data. In both the coronal and wind-shock models a substantial amount of wind attenuation of the X-ray and EUV photons is expected, so the logical next step is to incorporate this wind attenuation into the models. A modest wind optical depth does not affect the harder X-ray photons, but should have the effect of reducing the predicted *EUVE* line fluxes.

Including wind attenuation in the models requires calculating the wind ionization balance, obtaining the photoionization cross sections, and specifying the spatial distribution of the emitting and absorbing material. We calculate the ionization balance in the stellar wind using the non-LTE ionization and radiation transfer code described in MacFarlane, Cohen, & Wang (1994). This codes includes the EUV/X-ray radiation field in the photoionization calculation. Indeed the EUV/X-ray radiation can be the primary determinant of the ionization balance in the thin winds of B stars. The results of our calculation for the wind of ϵ CMa indicate that helium is about 20% He II and metals are predominantly in their second, third, and fourth ionization stages. These calculations assume mass-loss rates near 10^{-8} $M_\odot$ yr^{-1} and an X-ray source that is distributed throughout the stellar wind. The wind is generally less ionized when the X-rays are confined to the base of the wind. The ionization fractions are probably accurate only to within a factor of 2 or 3 due to the uncertainty in the intrinsic photospheric flux level in the helium continuum (due to uncertainty in our knowledge of the interstellar helium column density) and, to a lesser extent, in the wind temperature.

We cannot use this code directly to fit data because of its complexity and running time. Instead we use a fixed ionization balance for all models of a given run. As Figure 4 shows, the ionized stellar wind has a very different cross section per particle than does a neutral medium. Helium provides the bulk of the opacity in the *EUVE* bandpass but other heavy elements are important sources of continuum opacity, especially in the X-ray regime. K-shell edges of the abundant ions of carbon, oxygen, and silicon can be seen in Figure 4. L-shell photoionization of metals is an important source of opacity in the wind below the carbon K-shell edges (on 54 eV $< E \lesssim$ 300 eV) if helium is mostly fully ionized—as it is in the stellar wind. This indicates that even if helium is much more ionized than we predict ($X_{\rm He\ III}/X_{\rm He\ II} \gtrsim 4$), the opacity between the He II and the carbon edges is not much different than in our models. We calculate the K-, L-, and M-shell bound-free photoionization cross sections using the Hartree-Fock method described in Wang (1991).

The assumed spatial distribution of the emitting plasma depends on which general model we consider. In the

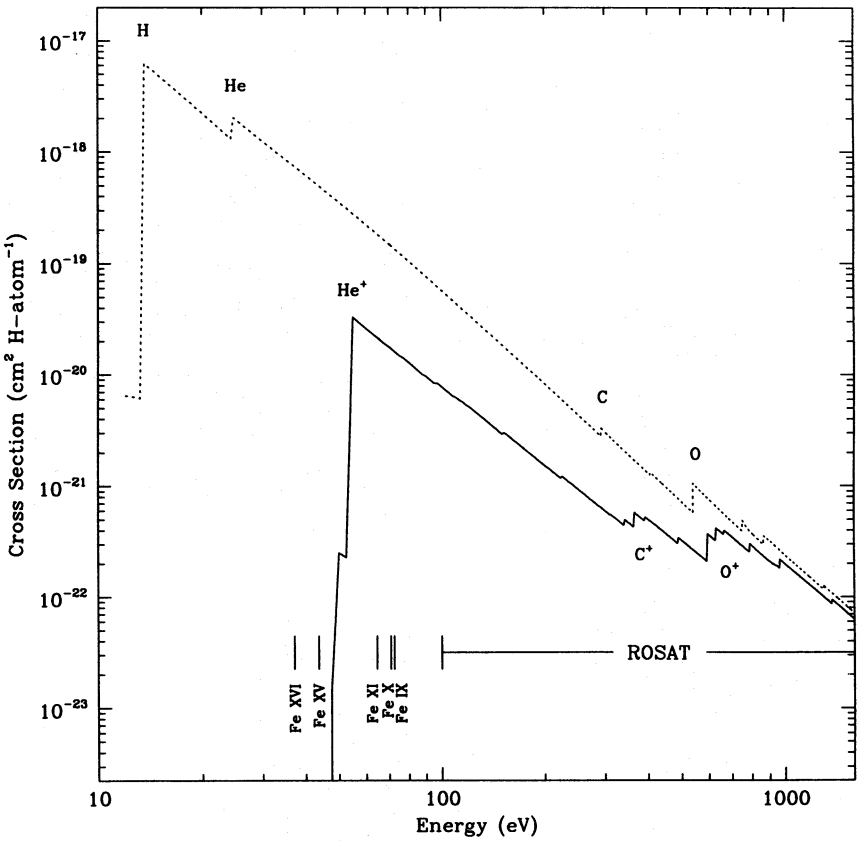

FIG. 4.—The cross section per hydrogen atom for the ions in the stellar wind (*solid line*) and for neutral elements in the interstellar medium (*dotted line*) is plotted vs. photon energy. It should be noted that while the interstellar medium has a much higher opacity per particle than does the wind material, the total column of material in the interstellar medium is, for ϵ CMa, much less than the wind column. Therefore above 54 eV the stellar wind is the primary source of opacity. The locations of the five detected EUV lines are indicated along the bottom of the plot, along with the *ROSAT* bandpass.

coronal model all of the emitting gas is confined near the surface of the star and the absorbing gas lies between the emitting material and the observer. For this case we use simple exponential absorption, in which the generated luminosity, L_λ given by equation (4), is multiplied by $e^{-\tau_\lambda(\text{wind})}$. Thus the emergent luminosity in the coronal emission plus wind absorption model is given by

$$L_\lambda^0 = e^{-\tau_\lambda(\text{wind})} \int Q(T)\Lambda(T, \lambda)dT \, . \quad (7)$$

Recall that Q, the differential emission measure, allows us to convert from a volume integral to a temperature integral.

In the wind-shock model the emitting and absorbing plasmas are interspersed and assumed to be distributed throughout the wind above some minimum radius, $R_0 \approx 1.5\ R_*$. To account roughly for self-absorption within the wind, we use an exospheric approximation, in which only the emission in the outer, optically thin wind contributes to the observed luminosity,

$$L_\lambda^0 = \int_{R_1(\lambda)}^{\infty} n_e n_H \Lambda 4\pi r^2 \, dr \, . \quad (8)$$

The lower limit of integration is taken here as the radius of unit radial optical depth, which, for a constant-velocity, spherical outflow is given simply by

$$R_1(\lambda) = \frac{\sigma_\lambda \dot{M}}{4\pi v \mu m_H} \, , \quad (9)$$

where σ_λ is the wavelength-dependent cross section per hydrogen atom, μ is the mean molecular weight per hydrogen atom, and m_H is the hydrogen mass.

The emergent luminosity, L_λ^0, can be compared to the total emitted luminosity,

$$L_\lambda = \int_{R_0}^{\infty} n_e n_H \Lambda 4\pi r^2 \, dr \, . \quad (10)$$

If we assume a smooth, constant velocity wind with $n \propto r^{-2}$ and further assume that a constant mass fraction of the wind is hot, then the fraction of the generated luminosity that is transmitted is given by

$$\frac{L_\lambda^0}{L_\lambda} = \frac{R_0}{\max\,[R_0, R_1(\lambda)]} \, . \quad (11)$$

We can express L_λ as a temperature integral (see eq. [4]) and so the luminosity in the wind-shock model using the exospheric approximation is given by

$$L_\lambda = \frac{R_0}{\max\,[R_0, R_1(\lambda)]} \int Q(T)\Lambda(T, \lambda)dT \, . \quad (12)$$

We take $R_0 \approx 1.5\ R_*$, which is roughly consistent with numerical simulations (Cooper 1994; Feldmeier 1995). Because the wind has reached an appreciable fraction of the terminal velocity by $r = R_0$ the assumption of $n \propto r^{-2}$ in the wind is justified.

Note that R_1, the radius at which optical depth equals unity, is a function of $\dot{M}/v$ and of wavelength through its dependence on the atomic cross section per particle in the stellar wind. Although the inclusion of wind attenuation makes the models much more realistic, both the exospheric and exponential absorption models add only a single additional free parameter, $\dot{M}/v_\infty$, to the overall emission models. Furthermore, the terminal velocity is known to better than a factor of 2 so that the only additional important free parameter is the mass-loss rate.

The result of fitting models with wind attenuation are as follows: The single-temperature model with wind absorption (either exponential or exospheric) does not provide a fit to the *EUVE* data. The two-temperature model with wind absorption gives a better *ROSAT* fit than the model with no absorption, having $\chi^2 = 16$ for 15 degrees of freedom ($\chi_\nu^2 = 1.07$), and it also fits the *EUVE* data. The two solution spaces do not intersect, however, meaning that there is no solution that can satisfy all of the data. The next most sophisticated model available is the power-law differential emission measure model with wind attenuation. This model has five free parameters, no more than the two-temperature plus wind attenuation has, but it is more realistic in that it allows for a continuous distribution of temperatures in the emitting plasma. Using the exponential absorption model we are not able to achieve a fit to the combined data sets, but using the exospheric models we are able to. In Figure 5 we compare the transmission as a function of photon energy for the exponential ($e^{-\tau_\lambda} = e^{-N\sigma_\lambda}$) and the exospheric $\{R_0/\max\,[R_0, R_1(\lambda)]\}$ models. There is more opacity in the soft X-ray regime with the exponential absorption model. This type of model is not able to fit the combined *EUVE* and *ROSAT* data sets because in order to provide the required attenuation of the EUV lines, the exponential absorption model alters the emergent X-ray spectrum too much. It should be noted that the EUV lines—only some of which are attenuated by the wind—constrain the temperature distribution in the gas which determines the X-ray spectrum. Therefore, a readjustment of the temperature distribution to make the model match the *ROSAT* data causes a mismatch between the model and the EUV lines.

The governing equation for the power-law emission with exospheric absorption model is

$$L_\lambda = \frac{R_0}{\max\,[R_0, R_1(\lambda)]} \, \text{EM}_X K \int_{T_{\min}}^{T_{\max}} T^\alpha \Lambda(T, \lambda)dT \, . \quad (13)$$

The free parameters are α, $T_{\min}$, $T_{\max}$, EM_X, and $\dot{M}$ (in $R_1[\lambda]$). The best-fit parameters for this model are shown in Table 5 along with the range of parameters as defined by the 90% confidence space based on the $\Delta\chi^2$ criterion for joint probability distributions ($\Delta\chi^2 = 9.24$ from Lampton et al. 1976). The combined solution is found for both of the two cases of interstellar opacity ($N_{\text{He I}} = 0.8 \times 10^{17}$ and $N_{\text{He I}} = 1.5 \times 10^{17}$), although the higher value of $N_{\text{He I}}$ gives a slightly better fit.

Note that the power-law slope is negative, although Figure 3 implies a positive slope. This difference is due to the neglect of wind attenuation in Figure 3. Now that we have derived the transmission of the wind as a function of photon energy we can correct the emission measure curves desired for each *EUVE* line for wind attenuation. We also convert the $EM(T)$ curves to an approximation of the differential emission measure by dividing $EM(T)$ by the characteristic temperature range over which each line is formed. We use half of the temperature of peak emissivity as this width. These corrected curves are shown in Figure 6 along with the differential emission measure we derive from the model fitting.

In order to produce these fits, we have to suppress the intensity of the Fe XIV 264 Å line and two silicon lines at 276

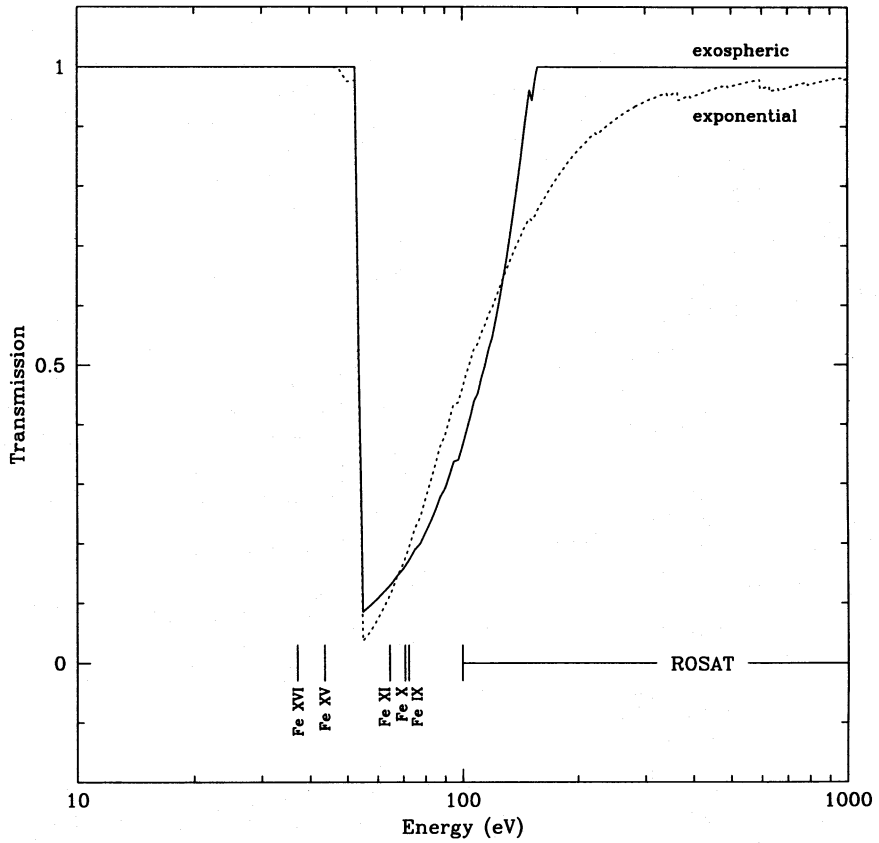

FIG. 5.—The transmission of the stellar wind for the two different attenuation models is plotted vs. photon energy. The EUV lines and *ROSAT* bandpass are indicated along the bottom of the plot. The models are normalized to provide the same degree of attenuation of the iron line complex near 175 Å.

Å and 317 Å in the models. A decrease, with respect to cosmic abundances, of the silicon abundance relative to iron in B stars has been previously noted by Gies & Lambert (1992). These authors found a mean decrease of about a factor of 2 with respect to cosmic abundances. We use a decrease of a factor of 3. The flux of the Fe XIV line at 264 Å would be decreased relative to the other strong iron lines if the density of the emitting plasma were lower than 10^{-9} cm^{-3} (Brickhouse et al. 1995). This is expected to be the case if the emission arises in the stellar wind where the density falls as $n \propto r^{-2}$ (see Fig. 7). So these adjustments to the models are reasonable if the emission arises in the stellar wind as opposed to a higher density corona, as the model predicts. For consistency, we recalculate all the previous models and compare them to the data making these same adjustments to the lines at 264 Å, 276 Å, and 317 Å. The values in Table 4 reflect these adjustments.

To further investigate the range of acceptable model parameters we refit the data several times assuming different ionization states for the stellar wind. We were able to get good fits to the data with models having ion mixtures ranging from $X_{\rm He\,II} = 0.05$ to $X_{\rm He\,II} = 0.30$. These values are within the range predicted in our ionization calculation given the uncertainty in the photospheric flux shortward of 504 Å. In Table 5 we show the best-fit values and the extent of the solution space for two wind ionization cases: $X_{\rm He\,II} = 0.1$ and $X_{\rm He\,II} = 0.2$. Using the higher wind ionization model ($X_{\rm He\,II} = 0.1$) does not affect the best-fit χ^2 values for the

TABLE 5

MODEL PARAMETERS FOR THE POWER-LAW MODEL WITH WIND ATTENUATION

	$X_{\rm He\,II}$[a] = 0.2		$X_{\rm He\,II}$[a] = 0.1	
PARAMETER	Best-Fit Value	90% Confidence Range (low:high)	Best-Fit Value	90% Confidence Range (low:high)
	$\chi^2 = 29$	$\chi^2 < 30.4$	$\chi^2 = 25$	$\chi^2 < 30.4$
α	−0.74	−0.77:−0.65	−0.87	−1.15:−0.45
log $T_{\rm min}$	5.7	5.7:5.7[b]	5.7	5.4[c]:5.7[b]
log $T_{\rm max}$	6.80	6.80:6.80	6.85	6.75:6.95
EM_X	7.0×10^{53}	6.4×10^{53}:7.0×10^{53}	6.8×10^{53}	6.5×10^{53}:7.8×10^{53}
$\dot{M}_{-8}/v_{1000}$[d]	2.80	2.80:3.05	5.8	4.1:7.6

[a] Combined solution space for the two ISM opacity models ($N_{\rm He\,I} = 0.8 \times 10^{17}$ and $N_{\rm He\,I} = 1.5 \times 10^{17}$).

[b] $T_{\rm min}$ was not allowed to exceed this value because the 171 Å line is seen in the data and it is formed in plasma of this temperature.

[c] Data are not sensitive to lower temperatures.

[d] Mass-loss rate in units of $10^{-8}\,M_\odot$ yr^{-1} over the terminal velocity in units of 1000 km s^{-1}.

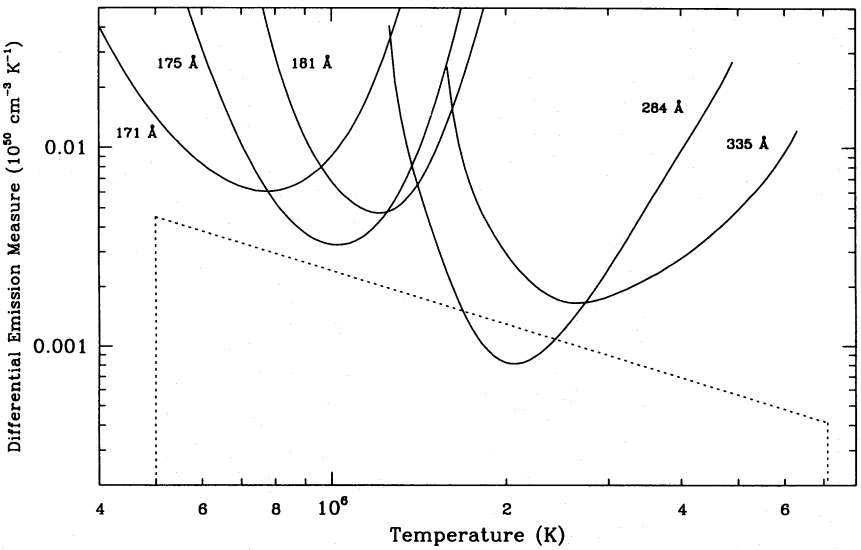

FIG. 6.—Upper limits to the differential emission measure derived from the five *EUVE* lines (*solid lines*) are shown along with the differential emission measure derived from the model fitting (*dotted line*).

one- or two-temperature models, but it does lead to a slightly better solution for the power-law plus absorption model and to a larger solution space for this model. The only significant difference in the derived parameter values is the mass-loss rate, which is higher by about a factor of 2 in the $X_{\rm He\,II} = 0.1$ case.

The reason that the solution spaces are similar for the two different cases is that they both have similar opacities in the important short-wavelength EUV and soft X-ray energy region (where helium is the dominant opacity source). In the case where there is less opacity per particle we find a higher mass-loss rate to bring the total optical depth in line with that in the model with more opacity per particle. Our model-fitting procedure constrains quite tightly the opacity decrement across the helium edge at 228 Å, but it cannot constrain very tightly the ionization balance in the wind.

5. DISCUSSION

In the previous section we developed a phenomenological wind absorption model which fit both the *ROSAT* and

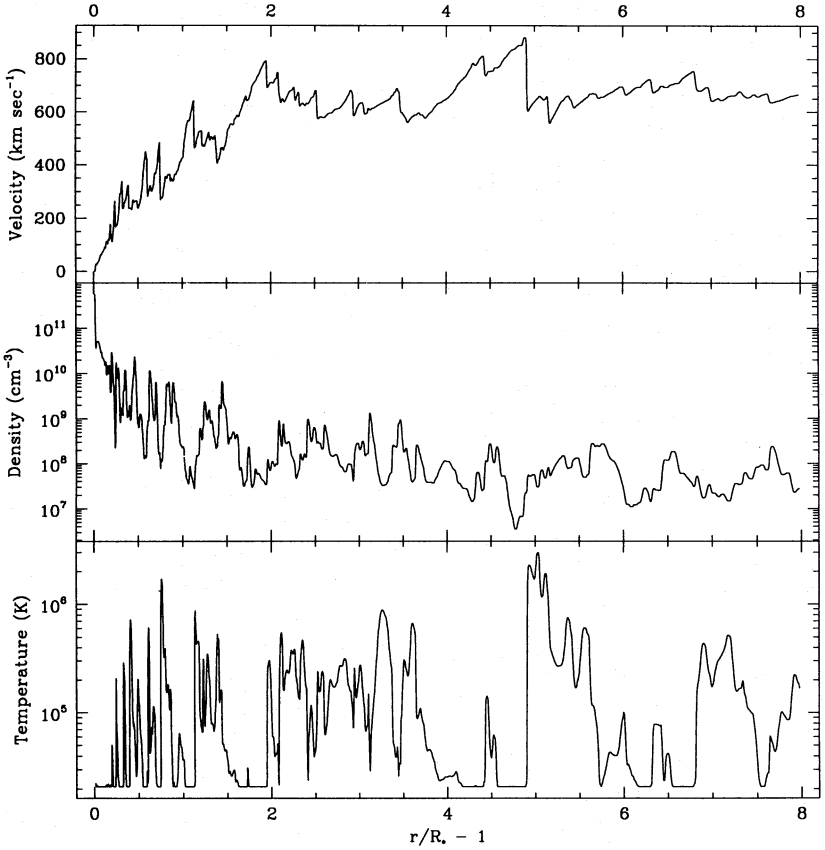

FIG. 7.—Snapshot of the velocity, density, and temperature profiles at $t = 3 \times 10^5$ from a numerical simulation of the radiation force instability in the wind of ϵ CMa.

EUVE data. Here we discuss the relative merits of the three general pictures of high-energy emission based on the model parameters we derived in § 4.4. We then present some exploratory hydrodynamical simulations of the wind instability. These are a first attempt to determine whether the wind instability alone is a sufficient explanation for the observed high-energy emission in ϵ CMa.

5.1. *Implications for the Three Emission Models*

The best observational discriminant among the coronal, wind shock, and external models is the degree of wind attenuation. No model without wind attenuation, even one with eight adjustable parameters, can fit the combined data sets. This is an argument against the applicability of the external model. In the exospheric approximation there is absolutely no wind attenuation for the external model. But a more complete treatment of the radiation transfer shows that a moderate amount of wind attenuation might be expected because hot material at large radii, but behind the star, emits photons which may be absorbed by cold wind material near the star. In the case of ϵ CMa this attenuation would be minimal—and certainly much less than is observed—because in the external model all of the material beyond about $1.6R_*$ will be hot, ionized, and therefore incapable of absorbing soft X-rays and EUV radiation (Drew et al. 1994).

The three detected iron lines between 170 Å and 180 Å (from stages $^{+8}$, $^{+9}$, and $^{+10}$) provide the strongest constraint on the degree of wind attenuation. In fitting the combined data sets we find that the fraction of emitted radiation at 175 Å (71 eV) that emerges from the wind is between 0.13 and 0.21 (90% confidence limits). Note that this degree of attenuation far exceeds that due to the interstellar medium, where $\tau(\lambda = 175\ \text{Å}) \approx 0.1$. The corresponding mass-loss rate ($2.8 < \dot{M}_{-8}/v_{1000} < 7.6$, including both the $X_{\text{He II}} = 0.2$ and the $X_{\text{He II}} = 0.1$ cases) is consistent with the predictions of line-driven wind theory ($\dot{M} \approx 6 \times 10^{-8}$, Abbott 1982; Kudritzki et al. 1989) and with the value based upon the 304 Å and 374 Å lines ($\dot{M} \approx 2 \times 10^{-8}$, MacFarlane et al. 1996). The upper limit on $\dot{M}/v_\infty$ implies that the wind is optically thin above about 215 eV. The lower limit implies 145 eV. If the emitting material lies mostly near the star's surface, as in the coronal model, the $\tau(\lambda = 175\ \text{Å})$ value implies a mass-loss rate of only $\dot{M} \approx 10^{-9}\ M_\odot\ \text{yr}^{-1}$, well below the predicted and observed values. An additional argument against the coronal model is that the only solutions are achieved with the exospheric, rather than the exponential, absorption model. And a final hint about the unsuitability of the coronal model comes from the lack of significant flux in the Fe XIV 264 Å line. This indicates that the emission originates in a lower density ($n \lesssim 10^9\ \text{cm}^{-3}$) plasma, as is predicted for the shock zones in the numerical simulations, rather than in a higher density plasma ($n \gtrsim 10^{10}\ \text{cm}^{-3}$), as would be expected to exist near the stellar surface.

We can also compare the derived plasma temperature distribution with the trends seen in coronae of late-type stars. Late-type stars that have X-ray spectra fitted by power-law models almost always show flat or positive slopes which are often quite steep. There is typically a high-temperature cutoff at $T \gtrsim 10^7$ K, except in quiescent main-sequence F and G stars that have high-temperature cutoffs near a few million degrees (Schmitt et al. 1990). One explanation for the trends seen in the plasma temperature distribution in the coronae of cool stars is that the slope of the differential emission measure is inversely proportional to the radiative cooling function and so has a positive slope above $T \approx 10^5$ K (Antiochos & Noci 1986). This explanation presumably could also apply to the purported coronal zones on hot stars.

The power-law index we find for the temperature distribution on ϵ CMa, $\alpha \approx -0.9$, is more negative than all but one of the 147 late-type stars in the *Einstein* survey of Schmitt et al. (1990).[4] Similarly, the high-temperature cutoff that we find, $T_{\max} \approx 7 \times 10^6$ K, is lower than that seen in the coronae of cool stars (Schmitt et al. 1990). The lower bound of the low-temperature cutoff in the plasma temperature distribution on ϵ CMa is unconstrained by our data. Presumably the differential emission measure increases at least to the point where the radiative cooling curve has its peak emissivity (near $T = 10^5$ K).

One of the basic predictions of the phenomenological wind shock model is that only a small fraction of the stellar wind is hot at any given time. In order to quantify the fraction of the wind that has been heated to EUV/X-ray–emitting temperatures, we can relate the parameters EM_X and $\dot{M}/v_\infty$ to each other through the filling factor, EM_X/EM_W, where $\text{EM}_W = \int_{R_0}^{\infty} n_e n_H 4\pi r^2\, dr \propto (\dot{M}/v_\infty)^2$. The integral is solved assuming a smooth wind of constant velocity. We note that our approximation of a constant velocity wind beyond R_0 tends to overestimate the filling factor, because near $R_0 \sim 1.5$ the wind has only reached about half of the terminal velocity. Therefore the wind emission measure, $(\text{EM})_w$, is underestimated in our approximation by about a factor of 2.5 (for a beta velocity law with $\beta = 0.8$), and the filling factor is overestimated by the same amount. The filling factor of hot gas which is derived from the combined data sets is relatively small, $0.04 < \text{EM}_X/\text{EM}_W < 0.25$. Taking the beta velocity law into account implies that filling factors as low as 2% are consistent with the data. Note that EM_W may also underestimate the total wind emission measure because it does not consider the effect of clumpiness in the wind.

5.2. *Initial Calculation of a Dynamical Wind Model*

We have seen that the phenomenological model that best agrees with all of the data is the wind shock model. One advantage of this model, besides its good fit to the data, is that it has a sound physical basis—the radiation force instability. As we described in § 1, there are some technical problems with performing a full calculation of the stellar wind structure within the context of the wind instability. The two major current limitations are the numerical problems related to implementing radiative cooling and the restriction to one dimension for the radiation force calculation (Cooper 1994; Feldmeier 1995). Despite these limitations, preliminary calculations are useful because they give us a rough idea of the overall X-ray luminosity, the temperature distribution, and the spatial distribution of shocks in the wind of ϵ CMa.

In Figure 7 we show a snapshot of the wind velocity, density, and temperature profiles determined from one-dimensional hydrodynamical simulations of the wind of ϵ

[4] Schmitt et al. (1990) use the logarithmic definition of the differential emission measure so 1 must be subtracted from their derived values of α in order to compare them to the value we derive for ϵ CMa.

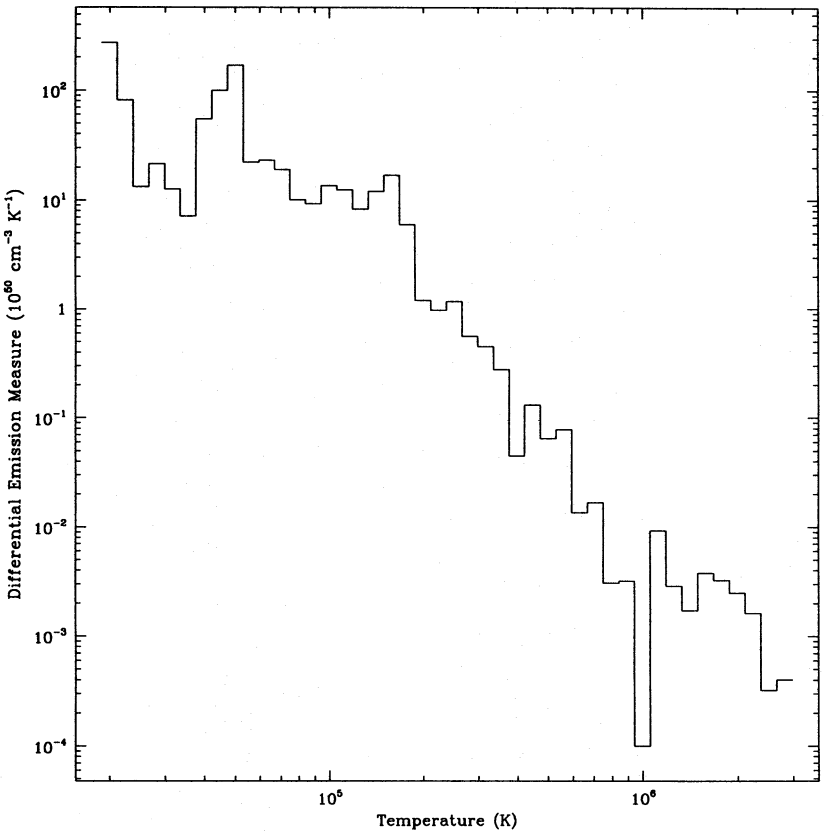

FIG. 8.—The temperature distribution for $r > 1.5\ R_*$ from the snapshot shown in Fig. 7. The distribution is weighted by the emission measure, which is proportional to $n_e n_H \times$ volume.

CMa using the methods outlined in Cooper (1994). As this figure shows, the wind is highly structured beyond a minimum radius, with many shocks distributed throughout. Most of the strongest shocks are reverse shocks in which rarefied, accelerated gas hits a slower, denser shell of material. In Figure 8 we show a histogram of the temperature distribution from the same simulation. We summed the hot gas in all of the spatial zones on the computational grid, putting each one into the appropriate temperature bin and weighting it by $n_e n_H \Delta V$.

It is quite interesting that, as in the above empirical shock model, the dynamical shock simulations yield a negative-slope power-law emission measure distribution with temperature. The result in Figure 8 is typical for our simulations of the wind of ϵ CMa, though the slope can vary between about -2 and -4. The highest temperature on the grid is determined by the velocity difference across the biggest shock front, and is typically a few million degrees in our simulations. The slope and the high-temperature cutoff in the simulations are thus similar to, but somewhat below, the values we derive from the *ROSAT* and *EUVE* data sets. The total emission measure of hot gas in these simulations is also consistent with the value derived from the observations. In the snapshot shown in Figures 7 and 8 the emission measure of gas hotter than log $T = 5.5$ is a few times 10^{53} cm^{-3}. The filling factor derived from the data shown in this figure is consistent with that found from fitting the combined data sets. Compare the differential emission measure shown in Figure 8 to that shown in Figure 6.

The agreement between the data and the numerical simulations is suggestive, though not definitive, considering the one-dimensional nature of the calculations and the fact that we have not explored the full extent of the simulation parameter space, including the lower boundary conditions. A limitation of the one-dimensional simulations is that there is not very much room for a large number of shocks in the wind because each shock must subtend a full 4 π steradians. This leads to a high degree of time variability of the EUV/X-ray luminosity in our simulations. This variability should be suppressed when full three-dimensional simulations can be performed. In three dimensions each shock can subtend a small solid angle and so many more separate shocks will exist than are seen in the one-dimensional simulations. Averaging over the large number of shocks will lead to a more constant total X-ray flux as individual shocks will grow and decay.

The simulations we present here do not include radiative cooling in the energy equation, due to the numerical difficulties discussed earlier (but see Feldmeier 1995 for an approximate solution to this problem). The successful inclusion of this term in the energy equation should lead to a flatter differential emission measure, more in line with what we derive from the data. This would also lead to a decrease in the total emission measure of hot gas, however. These changes might not be very great because hot, shocked gas primarily cools adiabatically in low-density winds (Cooper 1994). More detailed simulations must be performed in order to address these issues.

6. CONCLUSIONS

By combining *EUVE* and *ROSAT* observations of the early B giant ϵ CMa we are able to determine a narrow range of acceptable parameters for a phenomenological

wind emission spectral model. This emission model assumes a power-law distribution of temperatures, with high and low-temperature cutoffs in the emission. A spatial distribution of hot plasma in which some of the emitted photons are absorbed in the cool portion of the wind must also be included, and is accounted for using the exospheric approximation. These are the most detailed and realistic models which have yet been used to model high-energy observations of early-type stars, although they contain only one more free parameter than the more commonly used two-temperature equilibrium models. By including the *EUVE* data in the analysis we show that a temperature *distribution* and wind attenuation are both required, and we are able to constrain much more tightly the parameters than is possible with the *ROSAT* data alone.

We used these results to test the predictions of three general X-ray emission models. For the coronal model, the parameter values we derived are not consistent with the trends seen in coronae of cool stars: The X-ray spectrum is too soft, the distribution of temperature is skewed toward cooler plasmas, there is not enough wind absorption and that absorption is not of the right type. There is, however, too much wind attenuation of the EUV and X-rays for the emission to arise solely in a region external to the bulk of the stellar wind. The derived model parameters are most consistent with the predictions of wind-shock models. The degree of wind attenuation is the strongest piece of evidence for this. The filling factor we find is also consistent with predictions of the wind-shock model, with $\lesssim 10\%$ of the available wind emission measure being hot.

We also calculated some exploratory one-dimensional dynamical wind models based on the radiation force instability. These simulations produce a differential emission measure which qualitatively agrees with the parameters we derive from the data. The major discrepancy between data and model is the lack of variability in the data. This would be remedied if the simulations could be performed in three dimensions. Refinements to the wind instability simulations will be very valuable for exploring the ability of the radiation force instability to explain the EUV/X-ray emission observed in early-type stars.

The mass-loss rate we derive using the phenomenological wind model, $\dot{M} \approx 3\text{–}8 \times 10^{-8}\ M_\odot\ \mathrm{yr}^{-1}$, while consistent with theoretical predictions, is about 5 times greater than that derived from the *ROSAT* data by Drew et al. (1994). This is because in their picture, all of the wind beyond a certain radius is emitting X-rays (i.e., the filling factor is unity). In our picture only a small fraction of the wind material is emitting X-rays. In the analysis by Drew et al. (1994), the overall X-ray emission level governs the derived mass-loss rate, whereas in our analysis it is primarily the attenuation by the stellar wind which determines the derived mass-loss rate.

The luminosities of the *EUVE* detected lines are large and confirm, for the first time, the thermal nature of the high-energy emission seen in B stars. The luminosity emergent from the top of the stellar wind is close to 10^{30} ergs s^{-1} in each of the five lines. The line luminosities generated in the stellar wind are several times this value for the three lines near 175 Å. Each of these lines accounts for more than 10^{-9} of the bolometric luminosity of ϵ CMa. This is the first direct evidence that a very large fraction of the high-energy emission in early-type stars is emitted in the EUV, and therefore cannot currently be directly observed in most stars. These photons may in some cases make up the bulk of the high-energy photons which are produced and will play the primary role in determining the wind ionization balance in B stars.

The overall X-ray luminosity ($E > 100$ eV) we derived from the data is $L_X = 3.6 \times 10^{31}$ ergs s^{-1} ($L_X/L_{Bol} = 2.0 \times 10^{-7}$); with the emergent luminosity being $L_X^0 = 2.9 \times 10^{31}$ ergs s^{-1} ($L_X^0/L_{Bol} = 1.6 \times 10^{-7}$). Thus, about 80% of the X-rays which are generated escape the wind. The situation for EUV photons is quite different however. The EUV ($54 < E < 100$ eV) luminosity generated is $L_{EUV} = 1.4 \times 10^{32}$ ergs s^{-1} ($L_{EUV}/L_{Bol} = 8.0 \times 10^{-7}$), but only about 15% of this EUV emission escapes the wind. The absorbed photons heat and ionize the unshocked portion of the stellar wind, and most of them ultimately escape the wind in the form of 304 Å and 374 Å photons (MacFarlane et al. 1996). The observations reported in this paper are therefore evidence for the importance of the X-ray/EUV radiation field in setting the ionization balance in the wind. The fact that wind attenuation is important in this B star has implications for O stars as well. The O stars have higher mass-loss rates and because the attenuation scales as $\dot{M}/v_\infty$ in the exospheric approximation, O stars should have even more wind attenuation than we find for ϵ CMa. If this is the case then the $L_X/L_{Bol} \approx 10^{-7}$ law may not solely represent an intrinsic efficiency of the instability mechanism, but in fact may also be affected by the dependence of the total wind attenuation on mass-loss rate and hence on luminosity. Because earlier investigators almost always ignored wind attenuation of X-rays, the oft discussed quantity L_X/L_{Bol} is really L_X^0/L_{Bol}. The observed law is therefore $L_X^0/L_{Bol} \approx 10^{-7}$, whereas L_X/L_{Bol} should increase toward earlier spectral subtypes.

The star ϵ CMa is the only early-type star which has been detected in both the SW and MW spectrometers aboard *EUVE*. This is primarily due to the unusually small interstellar helium and hydrogen column densities along the line of sight. Because, as pointed out above, EUV photons play a central role in setting as well as diagnosing wind properties it is important that ϵ CMa be very well studied. We suggest that it be used as a standard B star for the purposes of wind and shock modeling. Future missions, with better spectroscopic throughput, might be able to detect several more B stars in the EUV. They will also be able to obtain a high-quality spectrum of ϵ CMa similar to those collected by *EUVE* for the late-type stars Procyon and Capella. In order to measure more than a dozen emission lines from ϵ CMa in a 100 ks exposure a detector effective area of about 10 cm^2 is required. This is a throughput 20 times greater than that of the *EUVE* medium wavelength spectrometer and is comparable to the throughput of the grating spectrometers planned for *AXAF-I*, which will have a resolution of $\lambda/\Delta\lambda \approx 1000$. Observations of ϵ CMa and other OB stars with this instrument will provide an enormous amount of information about the high-energy processes occurring on these stars.

We have benefited from many useful discussions with Mark Abbott of the Center for EUV Astrophysics, and with Myron Smith, John Finley, John Mathis, John Vallerga, and Craig Markwardt. This research was supported by NASA grants NAS 5-32646 and NAG 5-2282 to the University of Wisconsin.

REFERENCES

Abbott, D. C. 1982, ApJ, 259, 282
Abbott, M. J., & Friend, D. B. 1989, ApJ, 345, 505
Antiochos, S. K., & Noci, G. 1986, ApJ, 301, 440
Baade, D., & Lucy, L. B. 1987, A&A, 178, 213
Berghöfer, T. W., & Schmitt, J. H. M. M. 1994, A&A, 292, L5
Bohlin, R. C., Savage, B. D., & Drake, J. F. 1978, ApJ, 224, 132
Bowyer, S., & Malina, R. F. 1991, in Extreme Ultraviolet Astronomy, ed. R. F. Malina & S. Bowyer (New York: Pergamon), 397
Boyd, W., Jelinsky, P., Finley, D. S., Dupuis, J., Abbott, M., Christian, C., & Malina, R. F. 1994, Proc. SPIE, 2280, 280
Brickhouse, N. S., Raymond, J. C., & Smith, B. W. 1995, ApJS, 97, 551
Brown, A., Jordan, C., Stencel, R. E., Linsky, J. L., & Ayres, T. R. 1984, ApJ, 283, 731
Cassinelli, J. P., & Cohen, D. H. 1994, in Pulsation, Rotation, and Mass Loss in Early-Type Stars, ed. L. A. Balona, H. F. Henrichs, & J. M. LeContel (Dordrecht: Kluwer), 189
Cassinelli, J. P., et al. 1995, ApJ, 438, 932
Cassinelli, J. P., et al. 1996, ApJ, in press
Cassinelli, J. P., Cohen, D. H., MacFarlane, J. J., Sanders, W. T., & Welsh, B. Y. 1994, ApJ, 421, 705
Cassinelli, J. P., & Olson, G. L. 1979, ApJ, 229, 304
Cassinelli, J. P., Olson, G. L., & Stalio, R. 1978, ApJ, 220, 573
Cassinelli, J. P., & Swank, J. H. 1983, ApJ, 271, 681
Chlebowski, T., Harnden, F. R., & Sciortino, S. 1989, ApJ, 341, 427
Code, A. D., Davis, J., Bless, R. C., & Hanbury Brown, R. 1976, ApJ, 203, 417
Cohen, D. H., et al. 1996, in preparation
Cooper, R. G. 1994, Ph.D. thesis, Univ. Delaware
Corcoran, M. F., et al. 1993, ApJ, 412, 792
Corcoran, M. F., et al. 1995, ApJ, 436, L95
Cranmer, S., & Owocki, S. P. 1995, ApJ, 440, 308
Drew, J. E., Denby, M., & Hoare, M. G. 1994, MNRAS, 266, 917
Feldmeier, A. 1995, A&A, in press
Gies, D. R., & Lambert, D. L. 1992, ApJ, 387, 673
Grillo, F., Sciortino, S., Micela, G., Vaiana, G. S., & Harnden, F. R. 1992, ApJS, 81, 795
Gry, C., Lemonon, L., Vidal-Madjar, A., Lemoine, M., & Ferlet, R. 1995, A&A, in press
Gry, C., York, D. G., & Vidal-Madjar, A. 1985, ApJ, 296, 593
Hanbury Brown, R., Davis, J., & Allen, L. R. 1974, MNRAS, 167, 121
Harnden, F. R., et al. 1979, ApJ, 234, L51
Hartmann, L., Dupree, A. K., & Raymond, J. C. 1982, ApJ, 252, 214
Hearn, A. G. 1972, A&A, 19, 417
Hoffleit, D., & Jaschek, C. 1982, Bright Star Catalogue (New Haven: Yale Univ. Press)
Hillier, D. J., Kudritzki, R. P., Pauldrach, A. W., Baade, D., Cassinelli, J. P., Puls, J., & Schmitt, J. H. M. M. 1993, A&A, 276, 117
Kudritzki, R. P., Pauldrach, A., Puls, J., & Abbott, D. C. 1989, A&A, 219, 205
Lampton, M., Margon, B., & Bowyer, S. 1976, ApJ, 208, 177
Landini, M., & Monsignori Fossi, B. C. 1990, A&AS, 82, 229
Long, K. S., & White, R. L. 1980, ApJ, 239, L65
Lucy, L. B. 1982, ApJ, 255, 286
Lucy, L. B., & Solomon, P. M. 1970, ApJ, 159, 879
Lucy, L. B., & White, R. L. 1980, ApJ, 241, 300
MacFarlane, J. J., & Cassinelli, J. P. 1989, ApJ, 347, 1090
MacFarlane, J. J., Cohen, D. H., & Cassinelli, J. P. 1996, in preparation
MacFarlane, J. J., Cohen, D. H., & Wang, P. 1994, ApJ, 437, 351
MacFarlane, J. J., Waldron, W. L., Corcoran, M. F., Wolff, M. J., Wang, P., & Cassinelli, J. P. 1993, ApJ, 419, 813
Massa, D., Prinja, R. K., & Fullerton, A. W. 1995, ApJ, 452, 842
Meurs, E. J. A., et al. 1992, A&A, 265, L41
Mewe, R., Gronenschild, E. H. B. M., & van den Oord, G. H. J. 1985, A&AS, 62, 197
Morrison, R., & McCammon, D. 1983, ApJ, 270, 119
Mullan, D. J. 1984, ApJ, 283, 303
Nordsieck, K. H., Cassinelli, J. P., & Anderson, C. M. 1981, A&A, 248, 678
Nousek, J. A., & Lesser, A. 1993, *ROSAT* Newsletter, No. 8, p. 13
Owocki, S. P., Castor, J. I., & Rybicki, G. B. 1988, ApJ, 335, 914
Owocki, S. P., & Rybicki, G. B. 1984, ApJ, 284, 337
Pallavicini, R., Golub, L., Rosner, R., Vaiana, G. S., Ayres, T., & Linsky, J. L. 1981, ApJ, 248, 279
Pan, H. C., & Jordan, C. 1995, MNRAS, 272, 11
Pfeffermann, E., et al. 1987, Proc. SPIE, 733, 519
Porter, J., & Drew, J. E. 1995, A&A, 296, 761
Raymond, J. C., & Smith, B. 1977, ApJS, 35, 419
———. 1993, private communication
Rumph, T., Bowyer, S., & Vennes, S. 1994, AJ, 107, 210
Schmitt, J. H. M. M., Collura, A., Sciortino, S., Vaiana, G. S., Harnden, F. R., & Rosner, R. 1990, ApJ, 365, 704
Schmitt, J. H. M. M., Zinnecker, H., Cruddace, R., & Harnden, F. R. 1993, ApJ, 402, L13
Seward, F. D., et al. 1979, ApJ, 234, L55
Smith, M. A., Grady, C. A., Peters, G. J., & Feigelson, E. D. 1993, ApJ, 409, L49
Snow, T. P., & Morton, D. C. 1976, ApJS, 32, 429
Thomas, R. J., & Neupert, W. M. 1994, ApJS, 91, 461
Truemper, J. 1983, Adv. Space Res., 2, No. 4, 241
Uesugi, A., & Fukuda, I. 1982, Revised Catalog of Stellar Rotational Velocities (Kyoto: Kyoto Univ.)
Vallerga, J. V., Eckert, M., Sirk, M., Siegmund, O. H. W., & Malina, R. F. 1994, Proc. SPIE, 2280, 57
Vennes, S., Dupuis, J., Bowyer, S., Fontaine, G., Wiercigroch, A., Jelinsky, P., Wesemael, F., & Malina, R. 1994, ApJ, 421, 35
Waldron, W. L. 1984, ApJ, 282, 256
Wang, P. 1991, Ph.D. thesis, Univ. Wisconsin, Madison
Welsh, B. Y. 1991, ApJ, 373, 556